



Influence of the Spray Gun Type on Microstructure and Properties of HVOF Sprayed Fe-Based Corrosion Resistant Coatings

A. Milanti, H. Koivuluoto, and P. Vuoristo

(Submitted May 8, 2015; in revised form August 13, 2015)

The aim of this study is to evaluate the microstructural details and corrosion properties of novel Fe-based coatings prepared using two different generations of HVOF spray guns. These two generations of HVOF guns are Activated Combustion HVOF (AC-HVOF, 2nd generation) M2 gun and Supersonic Air Fuel HVOF (SAF, 3rd generation) M3 gun. Structural details were analysed using x-ray diffractometry and field-emission scanning electron microscope. Higher denseness with homogeneous microstructure was achieved for Fe-based coating deposited by the M3 process. Such coatings exhibit higher particle deformation and lower oxide content compared to coatings manufactured with M2 gun. Corrosion properties were studied by open-cell potential measurements and electrochemical impedance spectroscopy. The lower porosity and higher interlamellar cohesion of coating manufactured with M3 gun prevent the electrolyte from penetrating through the coating and arriving to the substrate, enhancing the overall corrosion resistance. This can be explained by the improved microstructures and coating performance.

Keywords corrosion behavior, Fe-based coatings, HVOF, structure

1. Introduction

Thermally sprayed Fe-based hardfacing and corrosion resistant coatings are being widely studied as cost-effective solutions and environmentally friendly alternatives to conventional thermally sprayed WC-Co and Ni-based coatings for wear and corrosion applications (Ref 1-6). Although thermally sprayed cermets and Ni-based coatings are known to have good wear and corrosion resistance (Ref 7), the price fluctuation of strategic metals such as Ni and Co and the inhalation toxicity problems related to Ni, Co, and WC (Ref 8, 9) has forced the research community to find alternative solutions. In such scenario, thermally sprayed Fe-based coatings are being extensively studied in order to improve the coating properties and make them a future alternative and reliable solution. Fe-based materials generally combine hard precipitates (carbides, borides) into an austenitic matrix with high chromium content in order to allow a formation of a thin and protective chromium oxide which in turn, enhances

the corrosion behavior (Ref 10). Many industrial processes (power generation industries, mining and construction, pulp and paper manufacturing, and general mechanical engineering) require high corrosion resistance in several conditions in order to increase lifetime of the component, lower costs, reduce inspection time and maintenance, and in turn increase throughput. Thermally sprayed Fe-based coatings may bring unquestionable benefits regarding low cost, high machinability, and high intrinsic material corrosion resistance. However, high density, oxide-free, and high interlamellar strength are among the most important issues faced in Fe-based corrosion resistant coatings as a solution for increasing the component lifetime in aggressive atmosphere. Especially in anodic protection, a dense coating acts as physical barrier which prevents the corrosive electrolyte to penetrate through the pores and particle boundaries towards the coating-substrate interface.

Several spraying processes have been used for Fe-based coating deposition over the last 40 years such as Arc Spraying (AS), Flame Spraying (FS), Air Plasma Spraying (APS), and High Velocity Oxygen Fuel spraying (HVOF). APS, AS, and FS are featured by high temperature, low particle velocity and the lack of a proper shrouding atmosphere which in turn resulted in large amount of molten particles with a non-uniform heating and solidification. This leads to low hardness, high oxide and porosity content up to 10% which in turn barely offers good protection against aggressive solution to penetrate towards the substrate (Ref 11-16). Although HVOF process has been extensively used for the Fe-based coatings due to its ability to deposit dense coatings with high adhesion

A. Milanti, H. Koivuluoto, and P. Vuoristo, Department of Materials Science, Tampere University of Technology, Korkeakoulunkatu 6, 33720 Tampere, Finland. Contact e-mails: andrea.milanti@tut.fi, heli.koivuluoto@tut.fi, and petri.vuoristo@tut.fi.

strength (Ref 1, 3, 6, 17, 18), some drawbacks are related to oxidation (due to the oxidizing atmosphere), tensile stress (in coatings compressive stress is preferred) and sometimes thermal deterioration due to the relatively high temperature of the HVOF flame (Ref 19, 20). Therefore, High Velocity Air Fuel spraying (HVOF) was later developed in order to overcome the above mentioned limitations of HVOF by reducing the operation costs, replacing pure oxygen with compressed air and to increase the flexibility of high velocity combustion spray processes while retaining their ability to produce superior coatings (Ref 21, 22).

HVOF is a rather new thermal spray process which consists of supersonic jet created by combustion of compressed air and fuel gases and subsequent expansion of combustion products through a convergent-divergent nozzle. Compressed air flows into a mixing chamber, where it is mixed with gaseous fuel. The mixture flows into a combustion chamber through multiple orifices of its catalytic ceramic wall. In the combustion chamber, the mixture is ignited by a spark plug, starting combustion. Within a second, the catalytic ceramic wall is heated above the auto-ignition temperature of the mixture, constantly activating its further ignition and combustion during the whole job cycle. Combusted gases flow into a convergent-divergent nozzle, where their speed reaches sonic velocity. Exhausting gaseous jet has a supersonic speed. Feedstock powders are fed axially into the combustion chamber. Three HVOF torch generations have been developed so far: 1st generation which ran with kerosene and air (AeroSpray gun, Praxair AF-3300 system), 2nd generation HVOF spray system (Quasar M2™ AC-HVOF, Uniquecoat Technologies Inc., Kermetico AK-07 Kermetico Inc.) and 3rd generation M3™ HVOF spray system (UltraCoat SAF, Uniquecoat Technologies Inc.) have optimized torch architecture and they mainly operate with combustion of air and hydrogen or mixture of hydrocarbons. The present work focuses on the microstructural details and corrosion properties of two Fe-based coatings manufactured with two latest generation states of HVOF spray guns (AC-HVOF, 2nd generation) M2 gun and Supersonic Air Fuel HVOF (SAF, 3rd generation) M3 gun as cost-effective and environmentally friendly solution in corrosion resistant applications.

In M3 HVOF torch, secondary air and fuel mixture is injected at the throat of the secondary nozzle in order to provide additional heat to the process. The M3 torch design together with high pressure capabilities assures higher particle velocities, higher powder feeding rate, lower temperature, and less oxidizing atmosphere (Ref 23, 24) resulting in a promising alternative method of manufacturing high quality metallic coatings (Ref 25). Low oxide content, high retention of powder microstructure, low porosity with an excellent wear, and corrosion behavior were reported in the recent studies of HVOF sprayed Fe-based coatings (Ref 26). Furthermore, equal or even better wear and corrosion resistance of HVOF-sprayed cermet coatings compared with HVOF-sprayed ones were reported (Ref 22, 27).

Although promising results in corrosion applications using HVOF sprayed Fe-based coatings have been

achieved (Ref 2, 19, 28), no research on the relation between HVOF torches and microstructure and corrosion behavior of HVOF sprayed Fe-based coatings has been performed yet.

2. Experimental Procedure

2.1 Materials and Coating Manufacturing

Gas-atomized ($-40+20\ \mu\text{m}$) Fe-based powder, Fe-31Cr-12Ni-3.6B-0.6C (wt.%) commercially traded as Durmat 512.021 (Durum Verschleiss-Schutz GmbH, Krefeld, Germany), was selected as feedstock material. Two HVOF guns were employed to spray the powder: Activated Combustion HVOF (AC-HVOF, 2nd generation) M2 gun and Supersonic Air Fuel HVOF (SAF, 3rd generation) M3 gun (Uniquecoat Technologies Inc., Oilville VA, USA). M2 gun was propane-fuelled with addition of hydrogen to further increase flame temperature. Regarding M3 gun, propane was used as main combustion fuel gas (propane gas 1) and as well as secondary combustion gas (propane gas 2) (additional combustion gas inserted into the nozzle). Low-carbon steel (Fe52) was used as substrate material. Substrates were grit-blasted (Al_2O_3 grits, 36 Mesh) prior to the spraying. The spray parameters are presented in Table 1.

2.2 Powder and Coating Characterisation

The microstructure and phase composition of the powder were studied by means of Scanning Electron Microscope (SEM, Philips XL30, FEI, Eindhoven, The Netherlands) equipped with energy dispersive x-ray (EDX) microanalysis and by x-ray diffractometry (XRD, Epyrean, PANalytical, Cu-K α radiation, The Netherlands), respectively. XRD experimental conditions were as follows: 2θ range 20° - 100° , step size 0.02° , scan speed $0.02^\circ/\text{s}$, fixed incident beam mask 10 mm, irradiated length 5 mm, nickel filter and PANalytical PIXcel 3D detector. Besides nickel filter, Fe fluorescence was further reduced by a proper selection of PHD values (30-80) for the diffracted beam. Phase identification was performed using the PANalytical X'Pert High Score Plus software using

Table 1 Spray parameters for HVOF processes

	HVOF spray gun	
	M2	M3
Sample name	Fe_M2	Fe_M3
Air (bar)	6.0	8.0
Propane gas 1, bar	5.4	7.3
Propane gas 2, bar	...	7.6
Hydrogen, L/min	25	...
Nitrogen carrier gas, L/min	40	60
Powder feeding rate, g/min	60	75
Stand-off distance, mm	150	300
Traverse speed, mm/s	1000	500
Step size, mm	3	4
Number of passes	6	6

the ICDD JCPDF-2 database (International Centre for Diffraction Data, Newtown Square, PA, USA). Particle size distribution was measured by a laser diffraction method using a wet dispersion technique (Sympatec laser diffraction system). The microstructure of HVAF sprayed coatings was observed using field-emission scanning electron microscope (FESEM, Zeiss ULTRApplus, Carl Zeiss Microscopy GmbH, Germany) and phase composition by XRD, under the same experimental conditions mentioned above. The microhardness of HVAF sprayed coatings was calculated by averaging 20 Vickers microhardness indentations on the polished cross sections by means of standard microindenter (Matsuzawa MMT-X7—300 g normal load).

2.3 Corrosion Test

Corrosion behavior of HVAF-sprayed coatings was evaluated with open-cell potential measurements (OCP) (customized test) and Electrochemical Impedance Spectroscopy (EIS) measurements (ASTM G3-14) in order to study existing through-porosity and the actual protectiveness of the coatings. Open-cell potential measurements (OCP) were performed by gluing a plastic tube (diameter 20 mm) to the coating surface. An amount of 12 mL 3.5 wt.% NaCl solution was filled into the tube. The open-cell potential was measured up to 24 days of immersion.

EIS is a powerful non-destructive electrochemical test which allowed collecting quantitative data by applying a small AC-potential to electrochemical cell. EIS was performed in 3.5 wt.% NaCl solution and the results have been represented through Nyquist and Bode representation at different time (up to 100 h) in order to evaluate the time-dependence of corrosion resistance. A model circuit has been chosen to fit the curves and to calculate the resistance to dissolution process. The testing conditions were the following: exposed surface 0.95 cm^2 , start frequency 300,000 Hz, end frequency 0.005 Hz, voltage perturbation amplitude $\pm 20 \text{ mV}$ around OCP measured for 300 s before EIS measurement.

Additionally, a customized combined electrochemical-cavitation test was employed in order to investigate further difference in protection mechanism behavior of studied coatings. The test aimed at evaluating the possible formation of protective oxide layer on tested coatings during immersion in 3.5 wt.% NaCl solution through the comparison of highly repassivating bulk material (tantalum) in such electrolyte.

Tested coating was mounted upwards in a vertical standard electrochemical cell in 300 mL of 3.5 wt.% NaCl solution (Fig. 1). A vibratory apparatus is placed inside the cell. The tip of a vibrating horn pulses in the electrolyte at a frequency of 20 kHz with amplitude of $50 \mu\text{m}$ producing a high concentration of micrometric bubbles towards the coating surface in the fluid kept at the temperature of about $20 \text{ }^\circ\text{C}$. The test consisted of two steps running sequentially (Fig. 2):

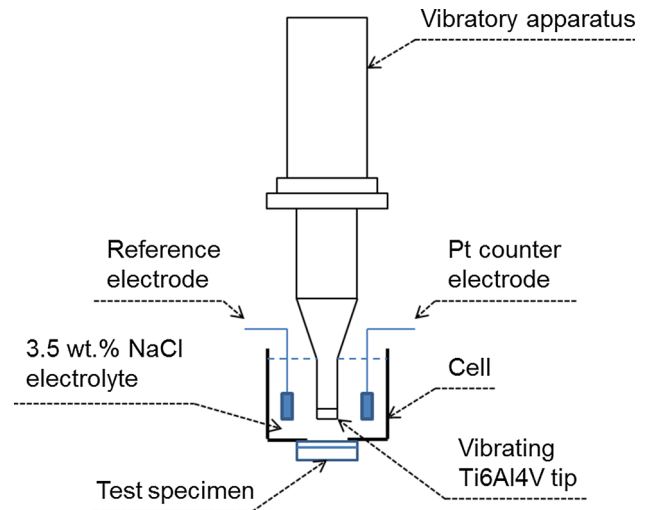
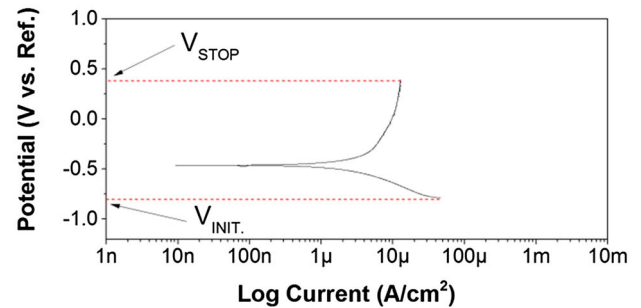


Fig. 1 Setup of customized combined electrochemical-cavitation test

Step 1: potentiodynamic polarization



Step 2: potentiostatic test (V_{STOP}) + cavitation

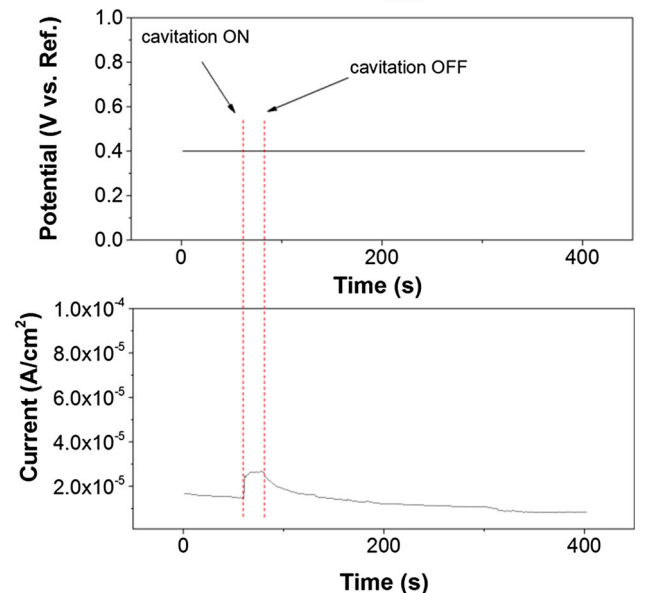


Fig. 2 Example of customized electrochemical test and possible results obtained (current density vs. time)

- *Step 1* potentiodynamic polarization (from -0.4 V versus OCP to an overpotential where the current density seems to stall—scan rate 0.5 mV/s (ASTM G3-14))
- *Step 2* potentiostatic test at the final potential (V_{STOP}) of potentiodynamic polarization. During potentiostatic test, when the current density stabilized, cavitation test was performed for 90 s. Current density was monitored throughout the potentiostatic test.

Tantalum bulk was chosen as reference material due to its large passivation voltage range in 3.5 wt.% NaCl solution in order to select the proper amplitude, frequency, and distance of the vibrating tip from the test specimen. Indeed, bubble flow impacting onto the test specimen should be high enough to break any protective layers but not too high to damage the coating material (cracks, particles pull-out). It is also worth underlining that the coatings were reported to have no mass loss up to 15 min of the same cavitation condition ruling out the occurrences of any damage (cracks, particles pull-out or material removal).

3. Results and Discussion

3.1 Microstructural Characteristics of Powder

Fe-based powder showed spherical shape, with low amount of satellites and rather smooth surface (indicative of good fluidity) (Fig. 3). Particle size distribution is narrow ($-40+20$ μm). Powder possesses a heterogeneous microstructure with large amount of acicular, long-shaped precipitates which EDS microanalysis revealed to be Cr-rich precipitates (Fig. 4, spectrum 1) embedded in a Fe-rich matrix (Fig. 4, spectrum 2).

Accordingly with cross-sectional SEM/EDS microanalysis, XRD measurement confirmed the presence of several intensity peaks which were assigned to chromium and iron mixed carbides $(\text{Cr,Fe})_{23}\text{C}_6$ (JCPDS 01-078-1500), chromium and iron mixed borides $(\text{Cr,Fe})_2\text{B}$ (JCPDS 01-072-1073) and chromium carbides Cr_7C_3 (JCPDS 01-089-5902), Cr_3C_2 (JCPDS 03-065-2427)

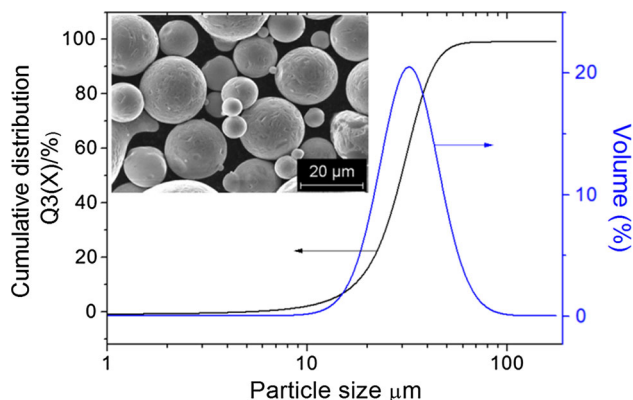


Fig. 3 Fe-Cr-Ni-B-C powder: morphology (SEM, SE image) and particle size distribution measured using laser diffraction

embedded in an austenitic (f.c.c.) Fe-rich γ matrix (JCPDS 00-03-0397) (Fig. 7). According to SEM cross-sectional image, it is noteworthy the large content of carbides and borides precipitations.

3.2 Microstructural Characteristics and Micromechanical Properties of Coatings

Both HVAF-sprayed coatings (Fe_M2 and Fe_M3) showed relatively dense microstructures (Fig. 5). However, it is clearly seen that Fe_M3 coating is thicker and has denser microstructure than that of Fe_M2. Fe_M3 coating (Fig. 6b) seemed to retain the powder microstructure better than Fe_M2 coating; long-shaped dark precipitates with similar size ($\approx 2-4$ μm length) were detected in the feedstock material (Fig. 4). Instead, microstructure of Fe_M2 (Fig. 6a) mainly consisted of particles with shorter long-shaped precipitates (compared to the original size of those present in the feedstock powder) surrounded by rounded sub-micrometric precipitations (bottom left corner of FESEM micrograph in Fig. 6a). A possible explanation might be found in lower flame velocity of M2 HVAF process which eventually results in higher particle dwelling time into the flame and in turn further increase of particle temperature when compared to M3 HVAF process. The larger heat provided to powder in M2 gun the higher amount of particle melting. Therefore, upon the impact the molten or semi-molten particles underwent rapid re-solidification to a finer metastable crystalline structure than that of the original feedstock powder.

Additionally, Fe_M2 is characterized by dark contours at the interfaces between partially melted particles which are much likely covered by thin oxide layer preventing a good interparticle interface (oxygen peak detected EDX Fig. 6a) which results in poorer particle bonding. Conversely, particle boundaries of Fe_M3 are barely visible

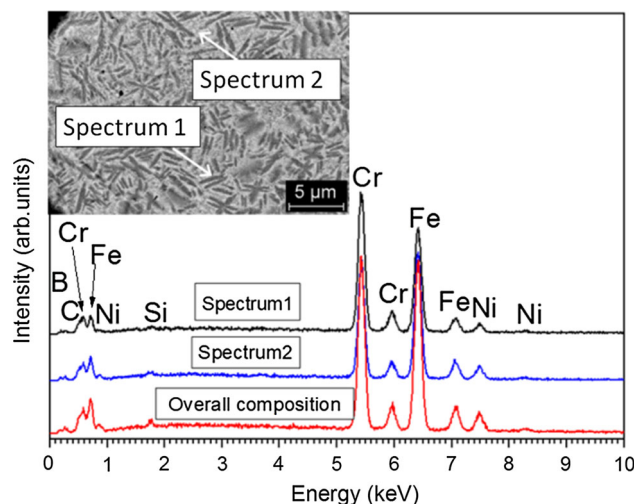


Fig. 4 Powder composition: EDX analysis from overall composition and spectrum 1 and 2 (powder cross-section, SEM, BSE image)

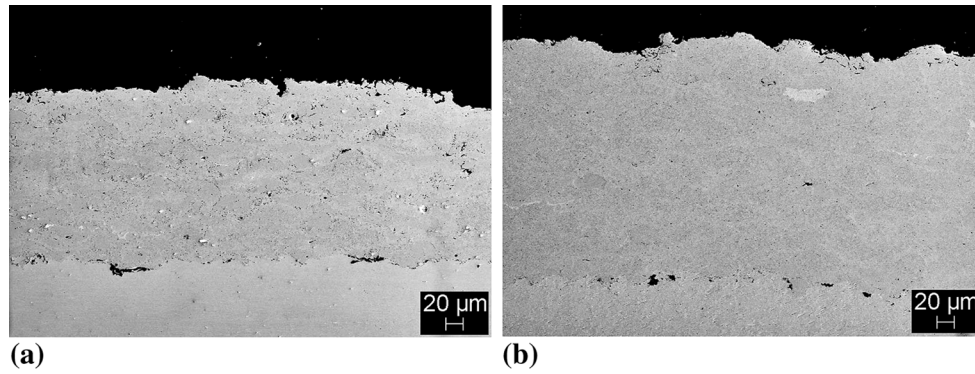


Fig. 5 Cross-sectional structure of HVOF (a) Fe_M2 and (b) Fe_M3 (FESEM, SE images)

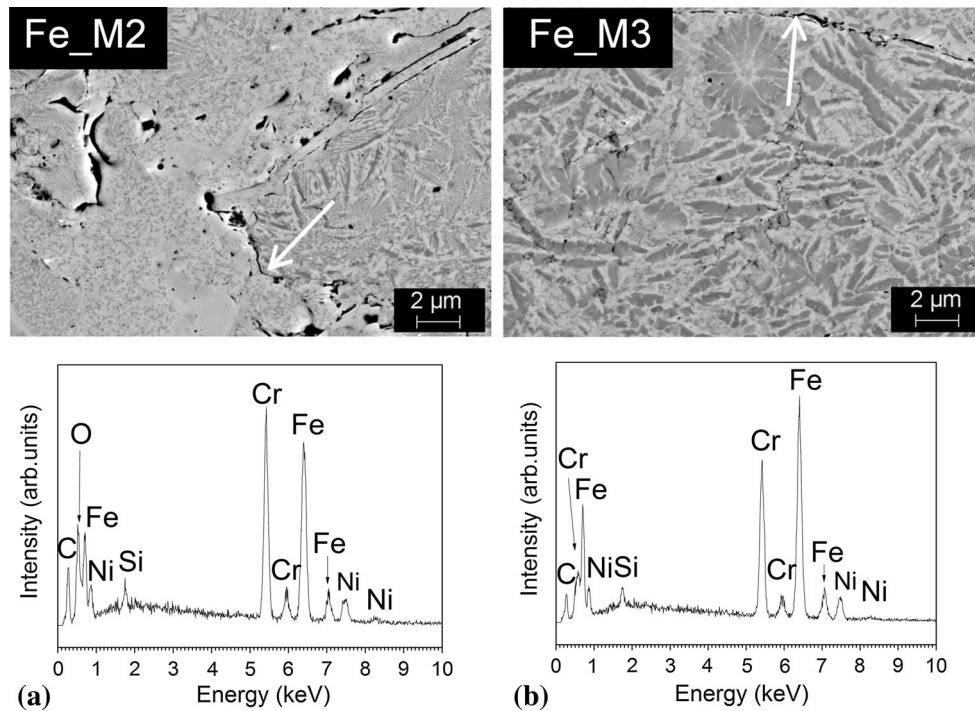


Fig. 6 Detailed structure and particle boundaries of HVOF (a) Fe_M2 and (b) Fe_M3 (FESEM images) and EDX spot analysis as indicated by white arrows

proving good inter-particles bonding (no oxygen peak detected in EDX Fig. 6b).

According to XRD patterns, both coatings seemed to mostly retain the microstructure of the powders and in turn avoid any detrimental reaction owe to intrinsic low temperatures of spraying processes. XRD patterns (Fig. 7) evaluation revealed the presence of austenitic (f.c.c.) γ matrix (JCPDS 00-03-0397) and several low intensity peaks were assigned to chromium and iron mixed carbides and borides (Cr_3C_2 03-065-2427, Cr_7C_3 01-089-5902, $(\text{Cr,Fe})_{23}\text{C}_6$ JCPDS 01-078-1500, $(\text{Cr,Fe})_2\text{B}$ JCPDS 01-072-1073). Most of the acicular Cr-rich precipitates probably correspond to this phases. Moreover, with regard to Fe_M2 coating the presence of Cr_2O_3 (JCPDS 04-008-6181) is assumed due to the increase of peak at $24.5^\circ 2\theta$. Instead in Fe_M3 XRD pattern, no peaks were attributed

to Cr_2O_3 , in accordance with EDX analysis on cross section (Fig. 6b—no oxygen peak detected). Although the coatings seem to retain the microstructure of powder, it is worth noting the slight peak broadening of highest intensity peak of austenite ($43.5^\circ 2\theta$) much likely due to the severe plastic deformation of the particles upon impact, and/or to particle melting and to the subsequent re-solidification. In both cases finer crystalline structure with microstrain are thought to induce peak broadening according to Scherrer formula (Ref 29). Further studies are needed in order to quantify microstrain and size of crystallites.

The Vickers microhardness of Fe_M3 coating was higher compared to Fe_M2 coating: $833 \pm 65 \text{ HV}_{0.3}$ versus $684 \pm 98 \text{ HV}_{0.3}$. Moreover, the lower standard deviation of Fe_M3 suggested more even microstructure. It is

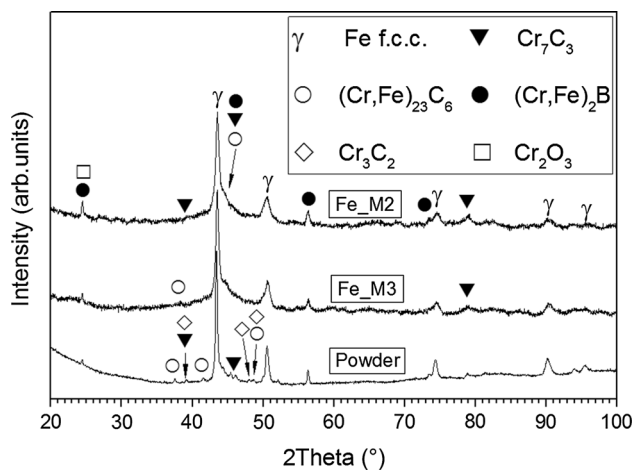


Fig. 7 XRD patterns of powder and coatings

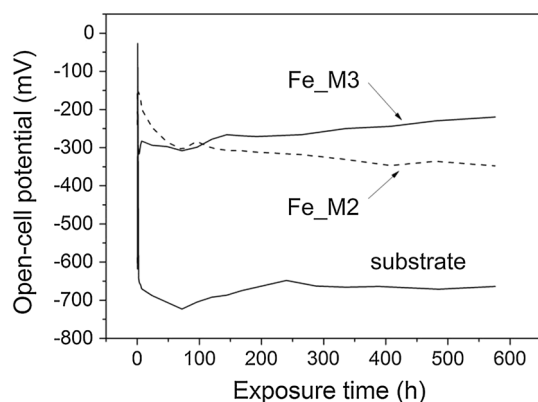


Fig. 8 Open-cell potential behavior of low-carbon steel substrate (Fe52), HVOF Fe_M2 and Fe_M3 coatings as a function of exposure time in NaCl 3.5 wt.% solution. Ag/AgCl reference electrode

generally acknowledged indentations at 3N load measure coating hardness which reflects the overall microscopic properties of the thermally sprayed coatings relying on intra-lamellar hardness (single particles material hardness) and on interlamellar cohesion to a greater extent (Ref 6). The changes in microstructure observed in SEM/EDS analysis (size of borides/carbides precipitates) (Fig. 6a and b) are thought to be not adequate to justify such change in hardness. Instead, the oxidized particle boundaries in Fe_M2 (Fig. 6a) seemed to play a remarkable role in decreasing the interlamellar cohesion and in turn the overall coating hardness. Similar behavior was described by Bolelli et al (Ref 30) highlighting the detrimental effect of oxide along splat boundaries. During indentation, these oxide strings may fracture allowing inelastic interlamellar sliding leading to larger indenter penetration and in turn lower microhardness.

3.3 Corrosion Behavior of Coatings

Open-cell potential (OCP) measurements were done in order to investigate the existence of through-porosity

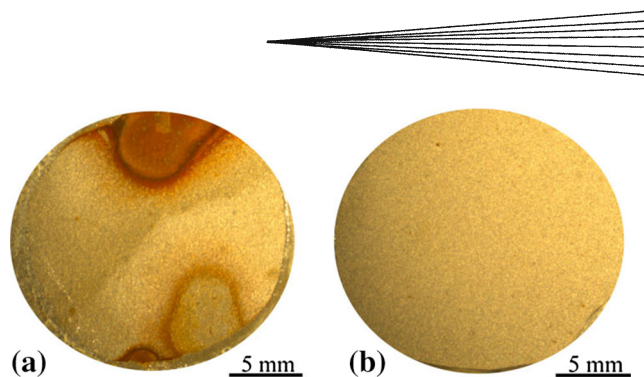


Fig. 9 Stereomicroscopy images of coating surface after 600 h exposure (a) Fe_M2 and (b) Fe_M3 coating

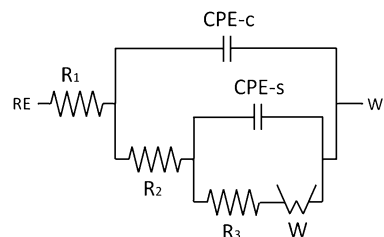


Fig. 10 Equivalent model circuit used to numerically describe corrosion resistance of coatings

(open-porosity) which allows the electrolyte to penetrate through the substrate and form detrimental and voluminous corrosion product at the substrate/ coating interface. Figure 8 shows OCP behavior of the coatings. At the very early stage of the test, the OCP set up at high potential values probably due to contaminations and/or thin oxide layer which rapidly formed on metallic polished surface. With time immersion, OCP of Fe_M2 steadily decreased, indicating open way for salt solution to penetrate towards the substrate and so a mixed potential between coating and Fe52 substrate was detected. Conversely, Fe_M3 seemed to stabilize its OCP at about -220 mV, suggesting impermeability up to 600 h immersion. At the end of the test, no corrosion products were detected on the Fe_M3 coating surface whereas Fe_M2 coating contained rust spots on its surface (Fig. 9).

EIS results have been represented through Nyquist and Bode representations at different time in order to evaluate the time-dependence of corrosion resistance. The hardest part to deal with in EIS is the choice of model circuit to achieve the best fit of data. By observing the Nyquist and Bode representations (Fig. 11 and 12), two time constants ($\tau_c = 1/\omega_c$) are observable (the one at high frequency characteristic of coating and the one at low frequency characteristic of low-carbon steel in the pores). In accordance to that an equivalent circuit was modeled (Fig. 10) in order to fit the data and describe electrochemical behavior of coatings.

R_1 represents the resistance of the electrolyte. It is important noting that even though a modern 3 electrode cells was used with a compensation for the solution resistance between the counter and the reference electrode, the solution resistance has always to be considered when model the circuit. The parallel subcircuit $CPE-c/R_2$

describes electrochemical behavior of coating whose open pores are filled by electrolyte. It is worth noting that CPE (Y_0, n) is a constant phase element which is generally employed instead of double layer capacitance in real electrochemical processes (Ref 26), whose impedance is expressed as following:

$$Z_{CPE} = 1/[Y_0(j\omega)^n], \quad (\text{Eq 1})$$

where j = the imaginary unit, $\omega = 2\pi f$ and f = the frequency, Y_0 and n = CPE parameters (when $n = 1$, the CPE becomes an ideal capacitance).

The second parallel subcircuit CPE- s/R_3 describes the double layer capacitance and charge transfer resistance at the electrolyte/working electrode interface. Specifically, R_3 is the charge transfer resistance and it represents the actual double layer current resistance at coating/electrolyte interface. W is the Warburg impedance added when equivalent circuit with mixed kinetic and charge transfer control is assumed.

The assumption of adding Warburg impedance is consistent with data achieved. In fact, Fe_M2 within 4 h showed a straight line with a slope of approximately 45° (Fig. 11a) suggesting a finite-thickness diffusion process

(Ref 20). The oxygen-rich particle boundaries, as reported in EDX (Fig. 6), may be oxides which eventually dissolve with the electrolyte and provide diffusion paths for the electrolyte to penetrate and corrode the substrate. The mixed kinetic and charge transfer control was deemed to be present up to 48 h due to the straight line at the end of semicircle at low frequencies in Nyquist representation (Fig. 11a) (characteristic of diffusion process). Although this diffusion process was not clearly observed in Fe_M3 (Fig. 11b) suggesting no electrolyte penetration through pits and particle boundaries, a slight diffusion was assumed due to the second time constant at low frequency appearing after 48 h immersion (Fig. 12b). By contrast, Fe_M2 showed a sharp change in electrochemical behavior. After 8 h immersion, the second time constant characteristic of mild steel substrate appeared and seemed to be dominant at 48 h immersion proving large electrolyte penetration (Fig. 12a).

The cross sections of Fe_M2 and Fe_M3 after 48 and 100 h, respectively, are shown in Fig. 13. It can be clearly seen how the electrolyte in Fe_M2 found a preferential path all along the particle boundaries whose oxide once dissolved left a free path for penetration causing a

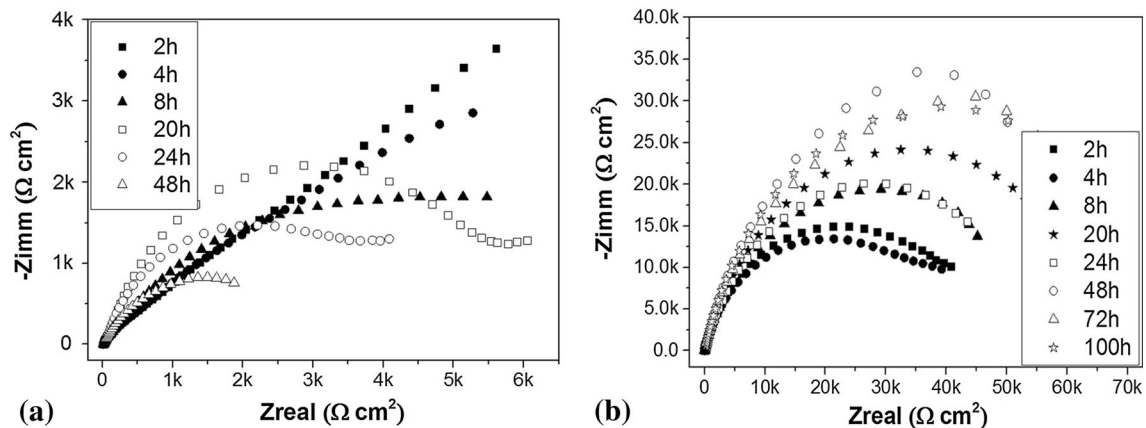


Fig. 11 Nyquist plot of HVAF (a) Fe_M2 and (b) Fe_M3 coatings

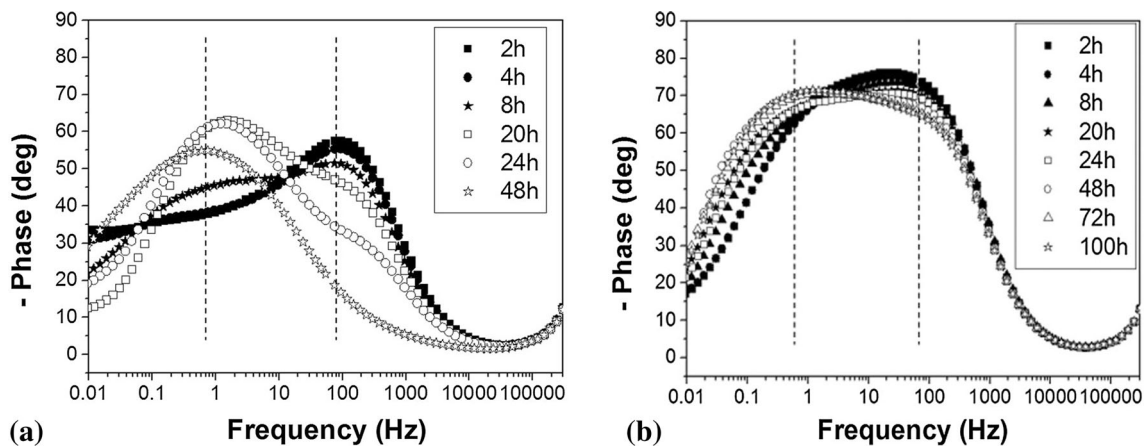


Fig. 12 Bode plot of HVAF (a) Fe_M2 and (b) Fe_M3 coatings

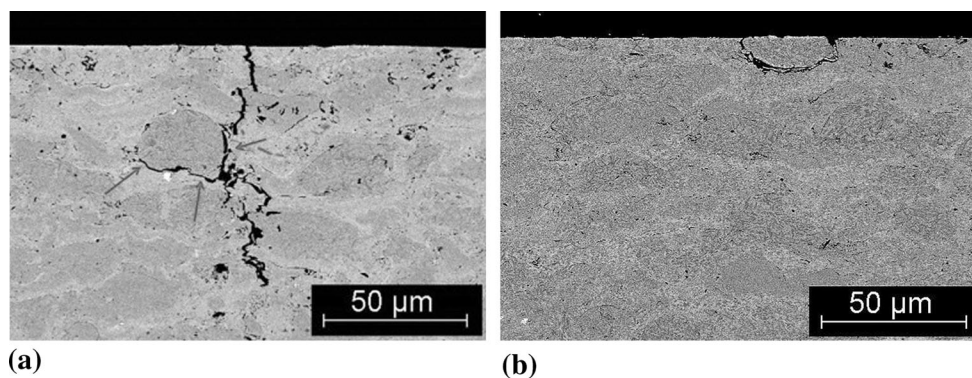


Fig. 13 Cross-sectional structures of HVAF (a) Fe_M2 and (b) Fe_M2 coatings after EIS test (SEM, BSE images)

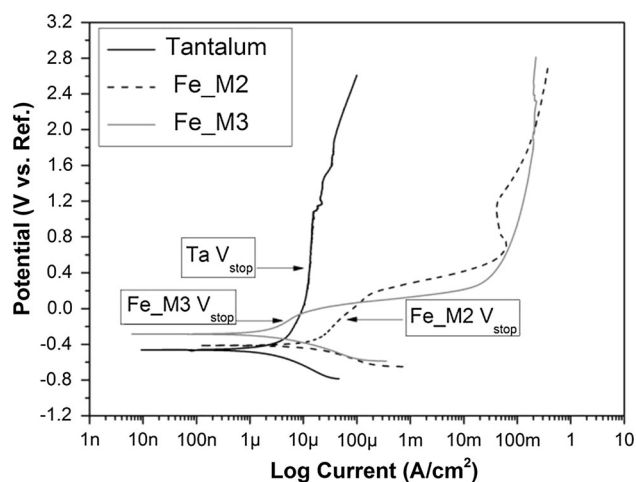


Fig. 14 Potentiodynamic polarization of HVAF Fe_M2, Fe_M3 coatings and Ta bulk as reference material in 3.5 wt.% NaCl solution

remarkable change in electrochemical behavior (Nyquist plot Fig. 11a, Bode plot 12a). Conversely, no visible through-paths were observed for Fe_M3. Only minor corrosive attacks were limited at the very superficial layers concerning very few loose particles.

In Table 2, the numerical values of E_{corr} , R_1 and R_3 are listed. With the exposed time, E_{corr} of Fe_M2 approaches that one of the substrate (Fe52 OCP ≈ -700 mV) and its corrosion resistance dropped to remarkably low value ($2.7 \text{ k}\Omega \text{ cm}^2$ after 100 h test) proving the insufficient protection and low coating impermeability. Conversely, Fe_M3 exhibited more even electrochemical behavior (Bode plot Fig. 12b), with a stable and nobler E_{corr} up to 100 h test. It is clearly noticed the small oscillation of E_{corr} and R_3 much likely due to passivation and depassivation during immersion suggesting the beneficial ability of repassivation of coating material also reported in other studies (Ref 20, 32). However, the noticeable increase of R_3 reported from 24 to 100 h is more likely due to the “plugging effect” caused by the accumulation of corroded products in defect or small pits of corrosion (Ref 2). Its stable E_{corr} together with high R_3 proved a proper

Table 2 E_{corr} , R_e CPE-c and R_{CT} calculated after data fitting

Exposed time, h	E_{corr}	$R_1, \Omega \text{ cm}^2$	$R_3, \text{k}\Omega \text{ cm}^2$
Fe_M2			
2	-328	14.94	67.5
4	-353	12.38	28.2
8	-394	15.22	8.3
20	-411	14.75	6.0
24	-413	14.42	4.4
48	-533	15.13	2.7
Fe_M3			
2	-231	14.11	51.5
4	-245	14.07	44.9
8	-274	14.06	55.7
20	-264	14.20	67.3
24	-269	14.18	56.2
48	-269	14.35	96.1
72	-294	14.23	70.0
100	-285	14.65	77.2

impermeability of the coating up to 100 h when sea water solution is used as aggressive environment.

In order to have a better understanding on the protection mechanism of Fe_M3 coating, a customized test was performed. Observing potentiodynamic polarization (Fig. 14), one can state no passivation in 3.5 wt.% NaCl solution is detectable in Fe-based coatings when compared with Ta reference material. However, both studied coatings showed a small track in anodic branch of current rate decrease approximately at a range of potential from -0.1 V versus OC to -0.4 V versus OC. Therefore, the following test was performed.

- (1) Open-cell potential was measured for 300 s;
- (2) Potentiodynamic polarization was performed from -0.4 V versus OC to an overpotential (V_{STOP}) where the current density seemed to slowdown;
- (3) Potentiostatic test at the V_{STOP} was performed for 600 s;
- (4) During potentiostatic test, cavitation test was performed for 90 s.

As reported in other reference (Ref 31), repassivating material such as Ta reference bulk showed a sharp in-

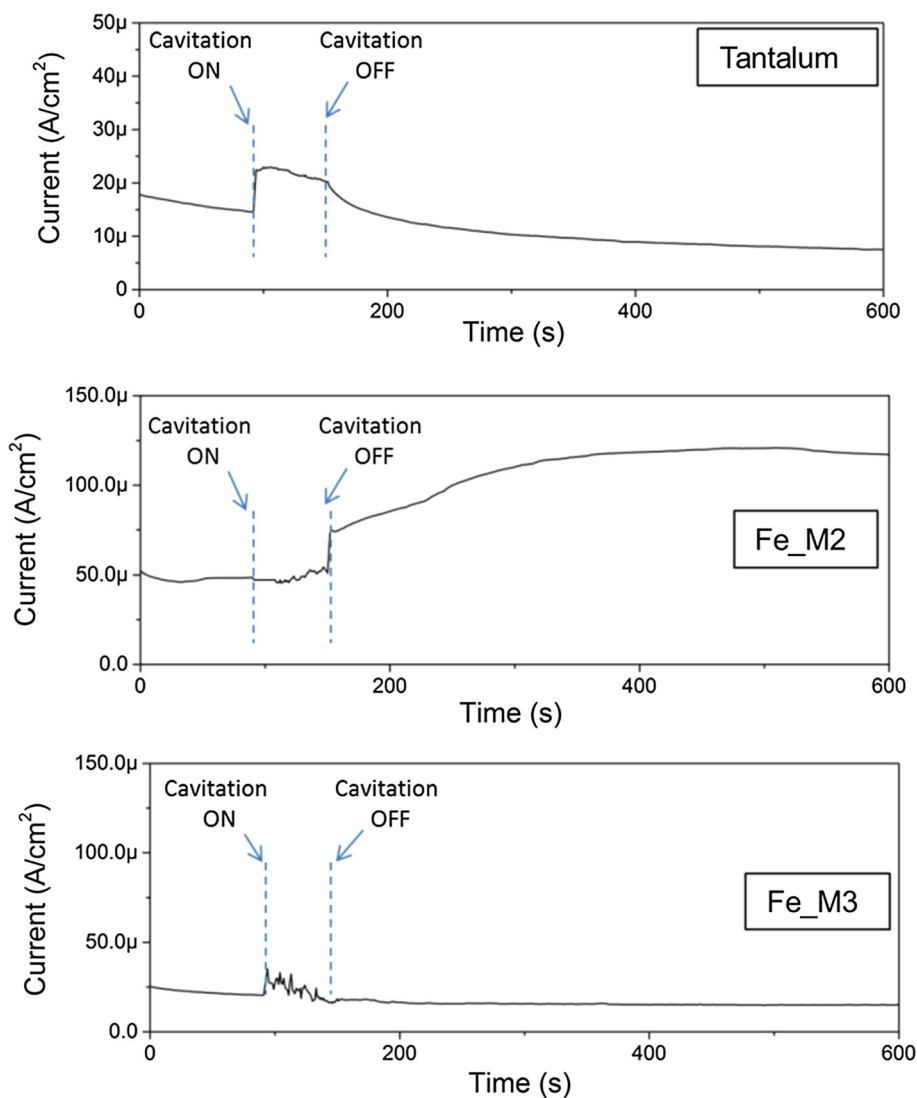


Fig. 15 Current density monitored during potentiostatic + cavitation test

crease of current density when cavitation turns on due to the rupture of the superficial oxide layer. Once cavitation is turned off, the current exponentially decreased to the same value of before the cavitation [characteristic current of oxide layer ($10\text{--}20 \times 10^{-6}$ A/cm²) (Fig. 15)]. No characteristic repassivation behavior was observed for both Fe-based coatings studied (Ta behavior—fast decrease of current density and exponential decrease towards oxide characteristic value of current density when cavitation is turn off).

Conversely, regarding Fe_M2, the current seemed to steadily increase after 90 s cavitation proving no protection. Most likely the corroded products formed into small defects or pits are thought to be porous and easily removable by the stream of bubbles resulting into an increase of current density. Instead, concerning Fe_M3 cavitation test seemed to have no effect on current density. The protection mechanism could be the “plugging effect” also according to the previous results (EIS, OCP).

Accumulation of corroded products in defects or small pits of corrosion (Ref 2) resulted in lower current density. Indeed, as also reported in other studies (Ref 26), the corrosion products are mainly made of iron oxyhydroxide FeO(OH). Such products are reported to form in pits or small defects and then hinder corrosion acting as physical obstacle to ionic diffusion and/or due to their reduced electronic conductivity.

4. Conclusions

HVAF sprayed Fe-based coatings were successfully deposited by means of two different gun generations. The higher performance of the latest Supersonic Air Fuel HVAF (SAF, 3rd generation) M3 gun together with a proper choice of spray parameters allowed a successful deposition of denser and harder Fe-based coating when



compared with coating manufactured with M2 gun. The crystalline phases of the powders were better retained in the coatings and no oxide phases have been detected conversely to the Fe-based coating manufactured with Activated Combustion HVAF (AC-HVAF, 2nd generation) M2 gun.

Electrochemical tests and OCP measurement proved the better protection provided by Fe_M3 coating due to lower current density and higher OCP which makes it nobler than Fe_M2. Moreover, corrosion products on Fe_M3 seemed to further increase corrosion resistance acting much likely as “plugging” products on the possible open pits in 3.5 wt.% NaCl test solution. Indeed, EIS measurements showed high corrosion resistance up to 100 h and a customized potentiostatic + cavitation test showed stable and low current density for Fe_M3.

HVAF M3 gun has the ability to better preserve the microstructural properties of feedstock material, to obtain lower oxide content at particle boundaries and in turn the better interparticle strength, higher Vickers hardness, higher denseness and impermeability, higher deposition rate and remarkably larger corrosion resistance. Such features make M3 gun a future process to further improve microstructural and mechanical properties of thermally sprayed Fe-based coatings as reliable alternatives to the more expensive and harmful WC- and Ni-based alloys.

Acknowledgments

The authors would like to thank Mr. Mikko Kylmälahti of Tampere University of Technology, Department of Materials Science for spraying the coatings and Mr. Khashayar Khanlari of Tampere University of Technology, Department of Materials Science for his assistance in the corrosion testing. The study was supported by the Finnish National Graduate School (Concurrent Mechanical Engineering) and Tampere University of Technology.

References

- Z. Zhou, L. Wang, F.C. Wang, H.F. Zhang, Y.B. Liu, and S.H. Xu, Formation and Corrosion Behavior of Fe-Based Amorphous Metallic Coatings by HVOF Thermal Spraying, *Surf. Coat. Technol.*, 2009, **204**, p 563-570
- R.Q. Guo, C. Zhang, Y. Yang, Y. Peng, and L. Liu, Corrosion and Wear Resistance of a Fe-Based Amorphous Coating in Underground Environment, *Intermetallics*, 2012, **30**, p 94-99
- B. Rajasekaran, G. Mauer, R. Vaßen, A. Röttger, S. Weber, and W. Theisen, Development of Cold Work Tool Steel Based-MMC Coating Using HVOF Spraying and Its HIP Densification Behaviour, *Surf. Coat. Technol.*, 2010, **204**, p 3858-3863
- A. Edrissy, T. Perry, and A.T. Alpas, Investigation of Scuffing Damage in Aluminum Engines with Thermal Spray Coatings, *Wear*, 2005, **259**, p 1056-1062
- C. Zhang, L. Liu, K.C. Chan, Q. Chen, and C.Y. Tang, Wear Behavior of HVOF-Sprayed Fe-Based Amorphous Coatings, *Intermetallics*, 2012, **29**, p 80-85
- G. Bolelli, B. Bonferroni, J. Laurila, L. Lusvardi, A. Milanti, K. Niemi, and P. Vuoristo, Micromechanical Properties and Sliding Wear Behaviour of HVOF-Sprayed Fe-Based Alloy Coatings, *Wear*, 2012, **276-277**, p 29-47
- L.M. Berger, Hardmetal as Thermal Spray Coatings, *Powder Metall.*, 2007, **50**, p 205-214
- G. Montavon, *Safety Issues and Risks Related to Thermal Spray Process*, ETSA Summer School Tampere University of Technology, Tampere, 2012
- Cobalt-Tungsten Carbide: Powders and Hard Metals; 12th Report on Carcinogens; U.S. Department of Health and Human Services, Washington, DC, June 10 2011
- S. Bose, *High Temperature Coatings*, Elsevier Inc., Burlington, 2007, p 299
- M.F. Morksa, Y. Tsunekawab, and M. Okumiyab, Characterization and Properties of Splats Sprayed with Different Cast Iron Powders, *Mater. Lett.*, 2004, **58**, p 2481-2485
- K. Vollenik, F. Hanousek, P. Chraska, J. Ilavský, and K. Neufuss, In-Flight Oxidation of High-Alloy Steels During Plasma Spraying, *Mater. Sci. Eng.*, 1999, **272**, p 199-206
- A. Edrissy, T. Perry, Y.T. Cheng, and A.T. Alpas, Wear of Thermal Spray Deposited Low Carbon Steel Coatings on Aluminum Alloys, *Wear*, 2001, **251**, p 1023-1033
- O. Redjdala, B. Zaidb, M.S. Tabtic, K. Hendad, and P.C. Lacazee, Characterization of Thermal Flame Sprayed Coatings Prepared from FeCr Mechanically Milled Powder, *J. Mater. Process. Technol.*, 2013, **213**, p 779-790
- B. Wielage, H. Pokhmurska, M. Student, V. Gvozdeckii, T. Stupnyckyj, and V. Pokhmurskii, Iron-Based Coatings Arc-Sprayed with Cored Wires for Applications at Elevated Temperatures, *Surf. Coat. Technol.*, 2013, **220**, p 27-35
- B. Fu, D. He, and L. Zhao, Effect of Heat Treatment on the Microstructure and Mechanical Properties of Fe-Based Amorphous Coatings, *J. Alloy. Compd.*, 2009, **480**, p 422-427
- Z.B. Zheng, Y.G. Zheng, W.H. Sun, and J.Q. Wang, Erosion-Corrosion of HVOF-Sprayed Fe-Based Amorphous Metallic Coating Under Impingement by a Sand-Containing NaCl Solution, *Corros. Sci.*, 2013, **76**, p 337-347
- A. Milanti, H. Koivuluoto, P. Vuoristo, G. Bolelli, F. Bozza, and L. Lusvardi, Microstructural Characteristics and Tribological Behavior of HVOF-Sprayed Novel Fe-Based Alloy Coatings, *Coatings*, 2014, **4**(1), p 98-120
- J.M. Guilemany, J. Fernandez, N. Espallargas, P.H. Suegama, and A.V. Benedetti, Influence of Spraying Parameters on the Electrochemical Behaviour of HVOF Thermally Sprayed Stainless Steel Coatings in 3.4% NaCl, *Surf. Coat. Technol.*, 2006, **200**, p 3064-3072
- R.Q. Guo, C. Zhang, Q. Chen, Y. Yang, N. Li, and L. Liu, Study of Structure and Corrosion Resistance of Fe-Based Amorphous Coatings Prepared by HVAF and HVOF, *Corros. Sci.*, 2011, **53**, p 2351-2356
- S. Liu, D. Sun, Z. Fan, H.Y. Yu, and H.M. Meng, The Influence of HVAF Powder Feedstock Characteristics on the Sliding Wear Behaviour of WC-NiCr Coatings, *Surf. Coat. Technol.*, 2008, **202**, p 4893-4900
- Q. Wang, S. Zhang, Y. Cheng, J. Xiang, X. Zhao, and G. Yang, Wear and Corrosion Performance of WC-10Co4Cr Coatings Deposited by Different HVOF and HVAF Spraying Processes, *Surf. Coat. Technol.*, 2013, **218**, p 127-136
- A. Verstak, V. Baranovski, Deposition of Carbides by Activated Combustion HVAF Spraying, *Thermal Spray 2004—Advances in Technology and Application—Proceedings of the International Thermal Spray Conference 2004*, 2004 (Materials Park, OH, USA), ASM International, p 551-555
- L.-M. Berger, R. Puschmann, J. Spatzier, and S. Matthews, Potential of HVAF Spray Processes, *Therm. Spray Bull.*, 2013, **6**(1), p 16-20
- A.P. Wang, Z.M. Wang, J. Zhang, and J.Q. Wang, Deposition of HVAF-Sprayed Ni-Based Amorphous Metallic Coatings, *J. Alloy Compd.*, 2007, **440**, p 225-228
- A. Milanti, V. Matikainen, H. Koivuluoto, G. Bolelli, L. Lusvardi, and P. Vuoristo, Effect of Spraying Parameters on the Microstructural and Corrosion Properties of HVAF-Sprayed Fe-Based Coatings, *Surf. Coat. Technol.*, 2015, **277**, p 81-90
- I. Hulka, V.A. Serban, I. Secosan, P. Vuoristo, and K. Niemi, Wear Properties of CrC-37WC-18M Coatings Deposited by HVOF and HVAF Spraying Processes, *Surf. Coat. Technol.*, 2012, **210**, p 15-20
- Z. Zeng, N. Sakoda, T. Tajiri, and S. Kuroda, Structure and Corrosion Behavior of 316L Stainless Steel Coatings Formed by

- HVAF Spraying With and Without Sealing, *Surf. Coat. Technol.*, 2008, **203**, p 284-290
29. B.B. He, *Two-Dimensional X-ray Diffraction, Chap. 12*, Wiley, Hoboken, 2009, p 426
30. G. Bolelli, T. Börner, F. Bozza, V. Cannillo, G. Cirillo, and L. Lusvardi, Cermet Coatings with Fe-Based Matrix as Alternative to WC-CoCr: Mechanical and Tribological Behaviours, *Surf. Coat. Technol.*, 2012, **206**, p 4079-4094
31. R.M. Fernandez-Domene, E. Blasco-Tamarit, D.M. García-García, and J. García-Antón, Repassivation of the Damage Generated by Cavitation on UNS N08031 in a LiBr Solution by Means of Electrochemical Techniques and Confocal Laser Scanning Microscopy, *Corros. Sci.*, 2010, **52**, p 3453-3464
32. J. Kawakita and S. Kuroda, Oscillational Corrosion Potential of HastelloyC Coatings Fabricated by GS-HVOF Spraying, *Corros. Sci.*, 2005, **47**, p 2053-2062